J. Fluid Mech. (2018), *vol.* 844, R2, doi:10.1017/jfm.2018.268

JFM RAPIDS
journals.cambridge.org/rapids

Experimental control of swept-wing transition through base-flow modification by plasma actuators

Srikar Yadala[1,2,†], Marc T. Hehner[1,3], Jacopo Serpieri[1], Nicolas Benard[2], Philipp C. Dörr[3], Markus J. Kloker[3] and Marios Kotsonis[1]

[1]AWEP Department, Section of Aerodynamics, Delft University of Technology, Kluyverweg 1, 2629HS Delft, The Netherlands

[2]Institut PPRIME, Université de Poitiers (CNRS UPR 3346, ISAE-ENSMA), Boulevard Marie et Pierre Curie, BP 30179, 86962 Futuroscope, France

[3]Institut für Aerodynamik und Gasdynamik, Universität Stuttgart, Pfaffenwaldring 21, D-70550 Stuttgart, Germany

(Received 14 November 2017; revised 26 February 2018; accepted 24 March 2018; first published online 13 April 2018)

Control of laminar-to-turbulent transition on a swept-wing is achieved by base-flow modification in an experimental framework, up to a chord Reynolds number of 2.5 million. This technique is based on the control strategy used in the numerical simulation by Dörr & Kloker (*J. Phys.* D: *Appl. Phys.*, vol. 48, 2015*b*, 285205). A spanwise uniform body force is introduced using dielectric barrier discharge plasma actuators, to either force against or along the local cross-flow component of the boundary layer. The effect of forcing on the stability of the boundary layer is analysed using a simplified model proposed by Serpieri *et al.* (*J. Fluid Mech.*, vol. 833, 2017, pp. 164–205). A minimal thickness plasma actuator is fabricated using spray-on techniques and positioned near the leading edge of the swept-wing, while infrared thermography is used to detect and quantify transition location. Results from both the simplified model and experiment indicate that forcing along the local cross-flow component promotes transition while forcing against successfully delays transition. This is the first experimental demonstration of swept-wing transition delay via base-flow modification using plasma actuators.

Key words: boundary layer control, boundary layer stability, instability control

1. Introduction

The swept-wing geometry gives rise to a three-dimensional laminar boundary layer, featuring the so-called cross-flow (CF). Cross-flow is a weak secondary flow

† Email address for correspondence: s.yadalavenkata@tudelft.nl

component, perpendicular to the outer inviscid streamline, caused by the relative imbalance between the pressure and inertial forces within the boundary layer. The CF component inherently forms an inflection point, which results in the inviscid cross-flow instability (CFI). This instability is characterised by co-rotating vortices of stationary (steady) or travelling (unsteady) nature, depending on external disturbances (Downs & White 2013). An extensive review on the topic has been compiled by Saric, Reed & White (2003).

Cross-flow instability has a pivotal role in the process of laminar-to-turbulent transition. As such, suppression of CFI presents a promising route towards transition delay and aerodynamic drag reduction (Joslin 1998). Different strategies have been proposed and investigated to control transition induced by stationary CFI modes. A brief review of these can be found in Serpieri, Yadala Venkata & Kotsonis (2017). A strategy that has received considerable attention is the use of discrete roughness elements (DRE), first proposed by Saric and co-workers (see Saric *et al.* (2003)) and later generalised as upstream flow deformation (UFD) by Wassermann & Kloker (2002). Primary stationary CFI modes appear in a selected band of unstable (or critical) spanwise wavenumbers and eventually undergo secondary instability leading to final transition (Saeed, Mughal & Morrison 2016). The DRE/UFD strategy is based on forcing shorter wavelength CFI modes (i.e. subcritical modes), which deter the growth of the critical mode, thus delaying transition. While initial wind-tunnel tests (Saric *et al.* 2003; Schuele, Corke & Matlis 2013) and numerical simulations (Wassermann & Kloker 2002) have shown successful transition delay, later flight tests (Saric *et al.* 2015) were inconclusive. Additionally, a recent study by Lovig, Downs & White (2014) indicated a dependency of the DRE performance on background roughness and baseline transition location. The aforementioned studies indicate a high sensitivity of the DRE/UFD technique to flow conditions, and particularly background disturbance levels (private communication with W. Saric).

An alternative CFI control strategy is based upon direct suppression of the inherent cause of the instability, which in this case is the CF component of the boundary layer. Numerical simulations employing wall suction (Messing & Kloker 2010) or body forcing (Dörr & Kloker 2015*b*), configured such as to suppress the CF component, were proven to delay transition. Dörr & Kloker achieved base-flow modification by applying a body force against the local CF. They observed a reduction in the amplification rates of both the steady and unsteady CFI modes, thus stabilising the boundary layer and yielding transition delay. An essential difference from the DRE/UFD approach is that base-flow modification relies directly on the suppression of the mean boundary layer, rendering its performance relatively independent of the nature of CFI (i.e. modes' wavelength and stationary or travelling type). However, to this point, the concept of base-flow modification for suppression of CFI has not been demonstrated experimentally.

In the present study, the base-flow modification strategy is demonstrated experimentally, by alternating current dielectric barrier discharge (AC-DBD) plasma actuators. Thorough reviews on plasma actuators and their applications can be found in Corke, Enloe & Wilkinson (2010), Wang *et al.* (2013) and Benard & Moreau (2014). While the application of AC-DBD actuators on two-dimensional boundary layers has been extensively studied, utilisation of these devices to control CFI is rather limited (e.g. Schuele *et al.* (2013), Dörr & Kloker (2015*b*), Shahriari (2016), Serpieri *et al.* (2017), Wang, Wang & Fu (2017)). Prior to the experimental investigation, a preliminary theoretical/numerical study is performed. The stability of the boundary layer, under the influence of the plasma body force, is numerically estimated using the simple

model proposed by Serpieri *et al.* (2017). Following the predictions of the model, experimental demonstration of the plasma-based base-flow modification is achieved by installing an AC-DBD plasma actuator that produces a two-dimensional body force, close to the leading edge of a swept-wing model. Two forcing conditions are investigated, namely forcing along and against the local CF. Infrared (IR) thermography is employed to visualise laminar-to-turbulent transition.

2. Methodology

2.1. *Experimental set-up and measurement technique*

The experiments were carried out in the closed-loop, Low Turbulence Tunnel (LTT) at TU Delft Aerodynamics (turbulence intensity $< 0.15\,\%$). The swept-wing model features an in-house designed airfoil shape (66018M3J), streamwise chord (c) of 1.27 m and a 45° sweep. Details of the employed swept-wing model and the wind tunnel are given in Serpieri & Kotsonis (2016) and Serpieri *et al.* (2017). The flow over the wing's pressure side was investigated. For this study, the wing incidence angle was set at $\alpha = 3°$. Experiments were performed for three free-stream velocities, namely $U_\infty = 25$, 27.5 and 30 m s^{-1}, corresponding to chord Reynolds numbers of 2.1, 2.3 and 2.5 million, respectively. The swept-wing reference system is referred to as xyz. It is such that its x axis is perpendicular to the leading edge, y axis is perpendicular to the chord plane and z axis is parallel to the leading edge. The corresponding velocity components are represented by uvw. The free-stream velocity is referred to as U_∞.

IR thermography was employed to inspect the laminar-to-turbulent transition front (Saric, Carpenter & Reed 2011; Serpieri *et al.* 2017). To enhance contrast, the swept-wing model was irradiated with six 1 kW halogen lamps, through glass windows in the test section. Surface temperature distributions were captured using an Optris PI640 IR camera with a thermal sensitivity of 75 mK, operating in the spectral band of 7.5–13 μm. Dewarping, deskewing and spatial calibration was applied in order to cast the raw images in the xz plane. After the temperature of the wing surface has reached an equilibrium, the camera registers 100 snapshots, at a rate of 5 Hz for every tested flow case. These are averaged in order to increase the signal-to-noise ratio. It should be noted that the results presented here are used to extract pertinent features of the flow topology, such as transition location. As such, no effort was made to correct the measured temperatures for emissivity and reflectivity effects.

In this study, stationary CFI modes were forced at a spanwise wavelength of $\lambda_z = 8$ mm which, for the tested flow conditions, is near the most unstable stationary mode as predicted by linear stability theory (LST). The choice for artificially forcing the critical CFI mode stems from a range of objectives. Most importantly, promotion of the critical mode presents a 'worst case scenario' for any given control scheme, thus ultimately giving a maximum bound on the performance of the control. Furthermore, for the studied flow conditions, natural (unforced) transition is downstream of the pressure minimum (located at $x/c \approx 0.63$, see Serpieri *et al.* (2017)) and is dominated by laminar separation. DRE forcing further assists in bringing transition upstream and achieving CFI-dominated conditions. Finally, by conditioning the initial amplitude of individual CF vortices, a more uniform and spanwise invariant transition front is achieved. An array of micron-sized DREs with diameter $d_{DRE} = 2$ mm and height $k_{DRE} = 60$ μm was employed to lock the critical CFI mode (Saric *et al.* 2003). The DREs were installed near the wing leading edge, at $x/c = 0.017$ (neutral point of $\lambda_{z,crit} = 8$ mm mode is at $x/c = 0.0068$). The ratio of DRE height and local displacement thickness is $k_{DRE}/\delta^* = 0.47$.

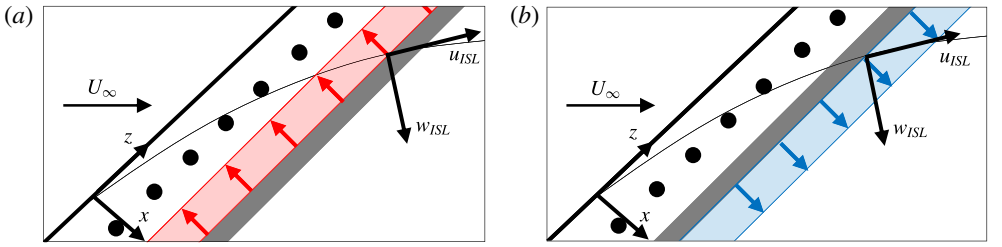

FIGURE 1. Schematic of the forcing mechanism (not to scale). Inviscid streamline (thin black line) and local velocity components (u_{ISL}, w_{ISL}). DRE arrangement (●) and plasma actuator exposed electrode (grey bar). (*a*) $-F_x$ plasma forcing (red arrows); (*b*) F_x plasma forcing (blue arrows).

2.2. *AC-DBD plasma actuator*

In the vicinity of the leading edge attachment line of a swept-wing, inviscid streamlines are almost aligned with the z direction. As such, forcing in the x direction will largely impact the CF component of the base flow. This is capitalised upon in the present study, where an AC-DBD plasma actuator that generates a spanwise invariant plasma forcing was designed. This design is adopted to avoid unwanted forcing of CFI modes as well as to ensure a simple and robust forcing configuration (figure 1).

Due to the extreme sensitivity of CFI to surface roughness (Saric *et al.* 2003), it was imperative to ensure minimum protuberance due to the actuator. With this goal in mind, computer-controlled spraying of micrometric conductive silver particles was employed to fabricate the electrodes, with thicknesses in the order of a few microns. 500 μm thick polyethylene terephthalate (PET) foils were used as dielectric material. The foils were wrapped around the leading edge and extended to $x/c = 0.69$ to form an uninterrupted smooth surface. The electrode width was $w = 5$ mm, on both sides of the dielectric, with no relative overlap or gap. Furthermore, AC-DBD actuators are known to impart unsteady fluctuations at the AC driving frequency, which can potentially trigger transition (Benard, Noté & Moreau 2017). This was observed in the study of Serpieri *et al.* (2017), which recommended forcing at higher frequencies (also discussed by Dörr & Kloker (2016)). Based on the above, forcing at $f_{ac} = 10$ kHz was employed for the present study. The actuator was installed such that the electrodes' interface was at $x/c = 0.035$. Two plasma actuators were fabricated, one to exert $-F_x$ forcing (figure 1*a*) and the second to exert F_x forcing (figure 1*b*) on the boundary layer. The air-exposed electrode was supplied with a sinusoidal AC signal of peak-to-peak amplitude between 5 and 9 kV, while the encapsulated electrode was grounded. The actuator was powered using a GBS Electronik Minipuls 4 high-voltage amplifier, controlled by LabView software.

It should be noted that the relative chordwise position of the DREs to the plasma actuator is not significant as long as they are positioned downstream of the first neutral point (to ensure the CFI is formed and growing). However, the position of the plasma actuator will affect its orientation with respect to the external streamline. Aligning the plasma body force to operate normal to the inviscid streamline is expected to enhance the effectiveness of the control, as this technique is based on attenuating the CF component.

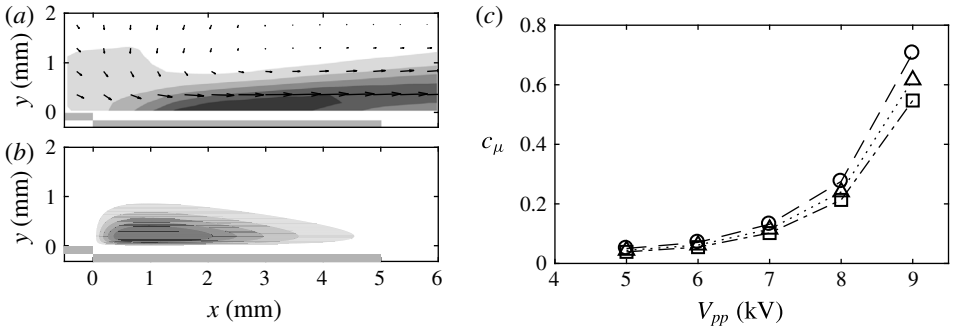

FIGURE 2. (*a*) Time-averaged induced velocity-magnitude field for $V_{pp} = 9$ kV, $f_{ac} = 10$ kHz (six levels from 0 (white) to 3 m s^{-1} (black)). The two grey lines below $y = 0$ depict the electrodes of the AC-DBD plasma actuator. (*b*) Body force computed using the empirical model by Maden *et al.* (2013) (six levels from 0 (white) to 3 kN m^{-3} (black)). (*c*) Variation of momentum coefficient c_μ with input peak-to-peak voltage V_{pp} (○: $U_\infty = 25$ m s^{-1}, △: $U_\infty = 27.5$ m s^{-1}, □: $U_\infty = 30$ m s^{-1}).

2.3. *Simplified plasma forcing model*

A number of parameters related to the flow and the AC-DBD actuator have an impact on boundary layer stability, which necessitates the definition of an efficient numerical model to carry out a preliminary assessment of the control effectiveness. With this objective, Serpieri *et al.* (2017) proposed a simplified model to demonstrate the effect of steady plasma forcing on boundary layer stability. This model is employed in the current study. An experimentally acquired, steady plasma body force (figure 2*b*) was included into the boundary layer solver as a source term (F_x/ρ) in the x-momentum equation. The steady two-dimensional incompressible boundary layer equations are solved to obtain the laminar boundary layer solution. This modified boundary layer yields the base-flow input for the linear stability solver, thus retrieving growth rates and N factors of the amplified CFI modes.

3. Results

3.1. *AC-DBD plasma actuator characterisation*

The time-averaged velocity field induced by the actuator used in the current study, when operated at $V_{pp} = 9$ kV, $f_{ac} = 10$ kHz is shown in figure 2(*a*). This field was acquired in a dedicated characterisation experiment using high-speed particle image velocimetry (PIV), in quiescent conditions (Serpieri *et al.* 2017). The corresponding body force (figure 2*b*) is computed using the empirical model proposed and validated by Maden *et al.* (2013). The body-force magnitude was calibrated such that the integrated body-force value matches the thrust calculated from the experimental velocity field using the momentum balance method (Kotsonis *et al.* 2011). The effect of two-dimensional forcing on the stability of the boundary layer was investigated by introducing this steady, volume-distributed plasma body force $F_x(x, y)$, $F_y = 0$ (see Maden *et al.* (2013), Dörr & Kloker (2015*a*)), into the boundary layer solver.

The integrated actuator thrust (T_x) is further used to compute the momentum coefficient c_μ by (3.1),

$$c_\mu = \frac{T_x}{\frac{1}{2}\rho u_e^2 \theta_u}, \tag{3.1}$$

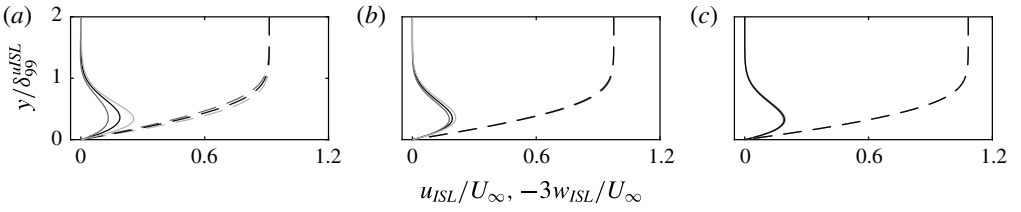

FIGURE 3. Computed boundary layer velocity profiles for $Re_c = 2.1 \times 10^6$ ($U_\infty = 25$ m s^{-1}), parallel (u_{ISL}: dashed line) and perpendicular (w_{ISL}: solid line, magnified by factor of three) to the local inviscid streamline at three chord locations, namely: (*a*) $x/c = 0.05$, (*b*) $x/c = 0.1$ and (*c*) $x/c = 0.3$. The three cases shown are: baseline (black), $c_\mu = -0.71$ (dark grey), $c_\mu = 0.71$ (light grey). The wall normal axis is non-dimensionalised with the boundary layer thickness based on $0.99 \cdot u_{ISL}$ from the local unforced profile.

where u_e is the local (at electrode interface) boundary layer edge velocity and θ_u is the local momentum thickness of the corresponding baseline case along the chordwise direction. The momentum coefficient c_μ is used to compare the actuator's authority for different flow conditions. The variation of c_μ with the input voltage for different free-stream velocities investigated in the current study is presented in figure 2(*c*). Henceforth, c_μ will be employed to discuss the different forcing conditions.

3.2. *Base-flow and stability modification*

The numerical boundary layer solutions at three different chord locations for the baseline (i.e. no forcing), $-F_x$ and F_x forcing cases are shown in figure 3. At the actuator's location, the external inviscid streamline angle is approximately 55° with respect to x. Thus, F_x forcing imparts momentum partially along the cross-flow and has an enhancing effect on both the streamwise and spanwise velocity components. Contrary to this, $-F_x$ forcing opposes both velocity components, thus diminishing their magnitude, as evident in figure 3. However, the profiles of the forced cases tend to collapse on the baseline flow case close to $x/c \approx 0.3$ (figure 3*c*). This is expected considering the low magnitude of the body force and its localised spatial extent, as shown in figure 2.

Stability diagrams for stationary CFI modes (i.e. zero frequency), indicating growth rates (α_i) and N factors, for the three tested cases shown in figure 3, are presented in figure 4. It is evident that the $\lambda_{z,crit} = 8$ mm mode (chosen as the mode forced by DRE in the experiment, indicated by the dashed line) is one of the most unstable stationary modes for these conditions. Comparing the stability plots of the baseline (figure 4*a*) and forced cases (figures 4*b* and *c*) confirms that $-F_x$ forcing hinders the growth of stationary CFI modes, thus stabilising the boundary layer. As expected, F_x forcing augments the growth rate of all stationary CFI modes and has a destabilising effect on the boundary layer. In both cases, the effect of forcing is rather local. Indeed, upstream of $x/c \approx 0.3$, the growth rates show insignificant disparity, as suggested by the almost identical velocity profiles at that station (figure 3*c*). However, the integral effect on the stability of the boundary layer, illustrated by the N factor, is evident well downstream of the forcing location. Assuming that the critical N factor does not significantly change due to actuation, the transition location can be expected to shift downstream with $-F_x$ forcing and upstream with F_x forcing.

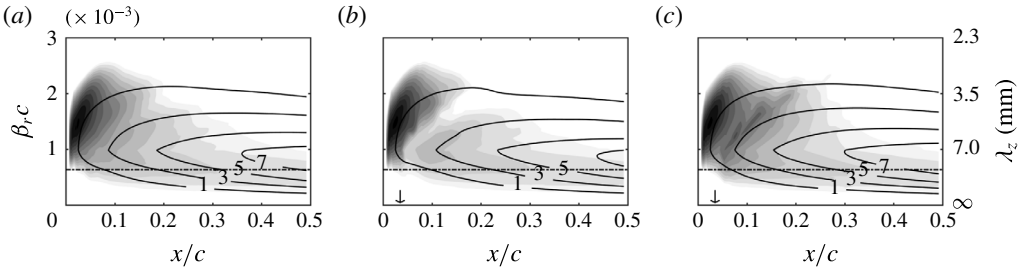

FIGURE 4. Streamwise amplification rate ($-\alpha_i c$) (15 levels from 0 (white) to 65 (black)) (spanwise wavenumber $\beta_r = 2\pi/\lambda_z$). Black contour lines show the amplification factor (N). Dash-dotted black line indicates the $\lambda_{z,crit} = 8$ mm mode. The three cases shown are: (a) baseline, (b) $c_\mu = -0.71$, (c) $c_\mu = 0.71$. Vertical arrows in (b) and (c) represent the location of the plasma forcing.

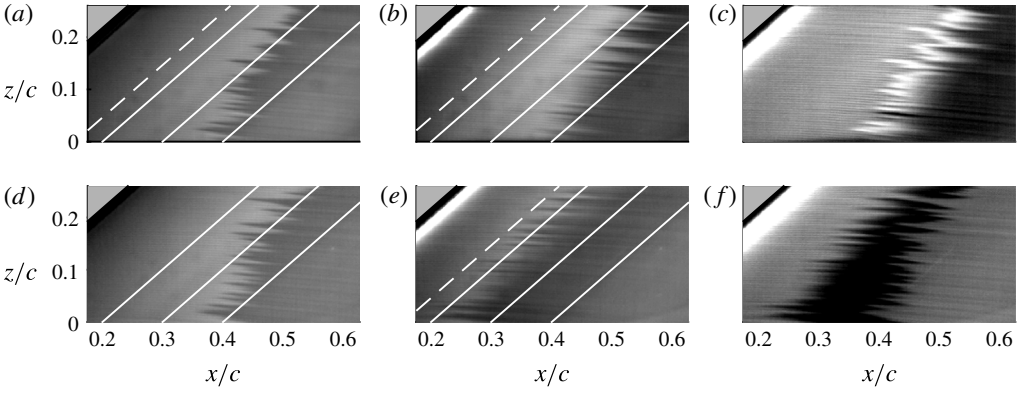

FIGURE 5. IR thermography mean fields ($Re_c = 2.1 \times 10^6$, $U_\infty = 25$ m s^{-1}). The flow comes from the left. The IR mean fields are dewarped and plotted in the xz plane. (a) Baseline. (b) $-F_x$ ($c_\mu = -0.71$). (c) Subtraction of (a) from (b). (d) Baseline. (e) F_x ($c_\mu = 0.71$). (f) Subtraction of (d) from (e). The solid white lines represent constant chord positions. Dashed line at $x/c = 0.15$ refers to figure 6(a).

3.3. *Thermal imaging of the flow topology*

The flow topology, visualised through IR imaging, is shown in figure 5 for $Re_c = 2.1 \times 10^6$ ($U_\infty = 25$ m s^{-1}). In the baseline (i.e. no forcing) cases shown in figures 5(a) and (d) the actuators configured for $-F_x$ and F_x forcing, respectively, are installed on the wing; however, they are not operative. The observed flow arrangement is the result of the steady forcing by the installed DRE. Spatial fast Fourier transform (FFT) analysis along constant chord lines shown in figure 6(a) confirms that the $\lambda_{z,crit} = 8$ mm mode forced by the DRE is indeed the spanwise dominant mode in the boundary layer. It should be stressed that no thermal calibration was performed on the recorded IR images. As such, the FFT analysis is only used to identify the spectral components and not the amplitude of CFI modes. To this effect, the wavenumber spectra presented in figure 6(a) are normalised with their respective maxima. Furthermore, in both baseline IR fields, the laminar breakdown occurs along

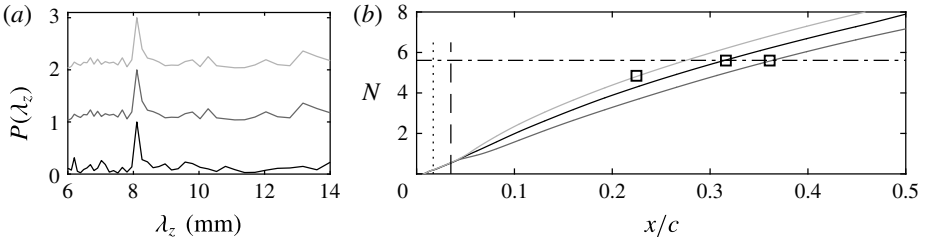

FIGURE 6. (*a*) Normalised wavenumber spectra along dashed line in figure 5(*a*), (*b*) and (*e*). Baseline (black line), $-F_x$ (dark grey), F_x (light grey). $-F_x$ and F_x cases are shifted by 1 and 2 for better visualisation. (*b*) N factors of the $\lambda_{z,crit} = 8$ mm stationary CFI mode. Location of DRE (dotted line) and location of plasma actuator (dashed line). Experimental transition locations (□). Baseline $N_{crit} \approx 5.6$ (dash-dotted line).

the characteristic jagged pattern reported for CFI-induced transition (Saric *et al.* 2003, 2011; Serpieri & Kotsonis 2016), at approximately the same chordwise position ($x/c \approx 0.32$).

The flow arrangement when $-F_x$ and F_x plasma forcing is applied is shown in figures 5(*b*) and (*e*) respectively. FFT analysis again confirms that the spanwise dominant mode in the boundary layer is the $\lambda_{z,crit} = 8$ mm mode forced by the DRE (figure 6*a*). In addition, to facilitate visualisation of the movement of the transition front, figures 5(*c*) and (*f*) show the subtraction of the IR field with plasma forcing from the corresponding baseline case. F_x forcing evidently shifts the transition front upstream, compared to the baseline case. Instead, $-F_x$ forcing, at the same conditions, shifts the transition front downstream.

3.4. *Transition location*

The evolution of N factors for the $\lambda_{z,crit} = 8$ mm stationary CFI mode along the chord, computed by the simplified model is presented in figure 6(*b*) (black curve). While the existence of other stationary CFI modes cannot be excluded, the 8 mm mode is the most dominant and observed to drive transition (figure 6*a*), as it is conditioned by the DREs. Hence, the N factors of only this mode are presented. In compliance with the stability diagrams (figure 4), the integral effect of local weakening or enhancement of amplification results in a global decreasing and increasing response on the N factors for $-F_x$ and F_x forcing, respectively. Using the transition locations obtained from IR thermography measurements (figure 5), the critical N factor for the baseline flow case is observed to be $N_{crit} \approx 5.6$. Due to the artificial decrease of N factors when $-F_x$ forcing is applied, the critical value N_{crit} at which transition naturally occurs in the baseline case is reached downstream, thus delaying transition. The increase in N factors with F_x forcing results in arriving at N_{crit} upstream of the baseline case, thus promoting laminar-to-turbulent transition. The experimentally detected transition locations of the forced flow cases are shown in figure 6(*b*), indicating the ability of the simplified modelling approach in capturing the overall trends of transition manipulation with forcing.

The aforementioned analysis can be extended to all tested cases, namely the variations in forcing momentum coefficient and Reynolds number. Experimentally measured transition locations extracted from the time-averaged IR fields are presented in figure 7, for both $-F_x$ and F_x plasma forcing. Transition delay or advancement is proportional to the magnitude of c_μ.

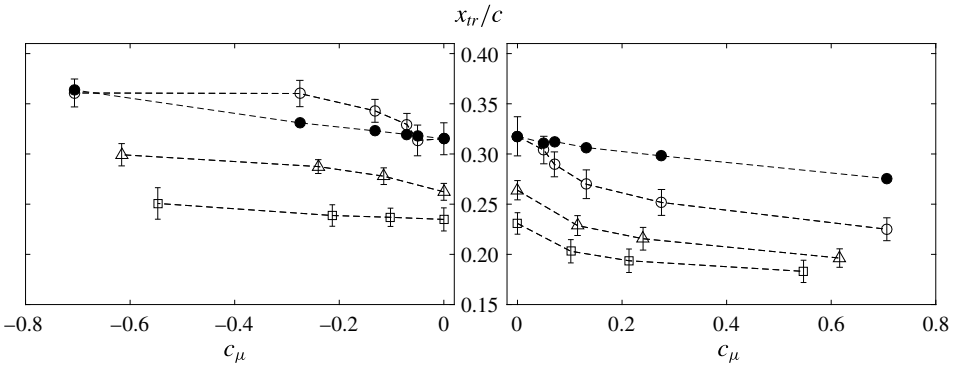

FIGURE 7. Experimentally measured transition locations (x_{tr}/c) versus momentum coefficient c_μ (○: $Re_c = 2.1 \times 10^6$, $U_\infty = 25$ m s^{-1}, △: $Re_c = 2.3 \times 10^6$, $U_\infty = 27.5$ m s^{-1}, □: $Re_c = 2.5 \times 10^6$, $U_\infty = 30$ m s^{-1}, ●: transition location predicted by the simplified numerical model for $Re_c = 2.1 \times 10^6$, $U_\infty = 25$ m s^{-1}).

Within the tested cases, the largest transition delay is approximately 4.5 %, occurring at the lowest Reynolds number and highest momentum coefficient tested. At higher Reynolds numbers, the displacement of the transition fronts with c_μ shows similar trends. For $Re_c = 2.3 \times 10^6$ ($U_\infty = 27.5$ m s^{-1}) (△), $c_\mu = -0.62$ and $Re_c = 2.5 \times 10^6$ ($U_\infty = 30$ m s^{-1}) (□), $c_\mu = -0.55$ the transition delay is 3.7 % and 1.6 %, respectively. The continuity in increasing the transition delay with $-c_\mu$ is well-defined; however, the percentage of delay decreases. Effectively, the current control technique is a direct approach against the weak CF velocity component. This component scales inviscidly with the free-stream velocity and thus, the authority of the applied body force on the boundary layer reduces as the Reynolds number increases (see variation of c_μ in figure 2*c*).

Furthermore, the critical mode in the boundary layer changes with the Reynolds number (as predicted by LST, not shown here); however, the applied forcing is observed to still have an effect. This further demonstrates the inherent insensitivity of the base-flow modification strategy to the wavenumber of the stationary CFI modes, in contrast to the UFD/DRE approaches.

The uncertainty bands in figure 7 represent the width of the transition-front, estimated by the standard deviation of the jagged transition-front. The transition-front width observed here appears rather insensitive to the plasma forcing. A possible reduction in the transition-front width would suggest the amplification of travelling CFI modes in the boundary layer, as these modes blur the transition-front to a more spanwise uniform arrangement (Downs & White 2013). This suggests that no fluctuations in the frequency band of travelling CFI modes were introduced, further confirming the recommendations of Serpieri *et al.* (2017) towards employing high AC driving frequencies.

The transition location for different c_μ predicted by the simplified model is also shown in figure 7. It is evident that the model is able to capture the experimental trend, but fails to predict the transition location accurately. This is expected, considering the range of assumptions and simplifications entering the chain of modelling steps (Serpieri *et al.* 2017). Notwithstanding the caveats brought forth, the simplified modelling approach presents a robust, fast and efficient tool, ideally suited for augmenting the experimental design process and providing basic, back-of-envelope scaling of the control performance.

4. Concluding remarks

The present study provides the first experimental proof of concept of plasma-based base-flow modification for CFI control. Nevertheless, several key points need to be addressed for the successful establishment of base-flow modification as a viable technique for the control of swept-wing boundary layers. A brief overview is given here. Cross-flow-dominated transition is known to be extremely sensitive to surface roughness effects (Saric *et al.* 2003, 2011, 2015). The DRE/UFD approach has shown promising results for control of CF-dominated transition; however, it also revealed the strong sensitivity of this technique to a number of parameters such as free-stream turbulence and background roughness (Lovig *et al.* 2014; Saric *et al.* 2015). While the base-flow modification strategy can be expected to be more robust to these effects, it also requires more energy to realise control of transition compared to the DRE/UFD strategy.

As mentioned earlier, any potential flow control system, aimed at swept-wing transition delay, needs to adhere to strict roughness and thickness thresholds. Although plasma actuators have been praised for their non-obtrusive character, conventional construction techniques typically followed in laboratory settings result in electrode thicknesses of tens of microns, which are prohibitive in the case of CF-dominated transition. In this study a prototype automated fabrication technique was developed to construct submicron metallic electrodes, which should be further developed, characterised and scaled. Furthermore, in Serpieri *et al.* (2017) plasma actuators were found to introduce velocity fluctuations in the band of travelling cross-flow instabilities. In the present study, the issue was circumvented by high AC driving frequency ($f_{ac} = 10$ kHz). However, upscaling this technique to higher Reynolds numbers will scale the frequency of instabilities as well. This will effectively require a further increase of the AC frequency, which will in turn challenge the current plasma generation approach. In addition, possible receptivity mechanisms between the plasma formation and incoming disturbances (i.e. free-stream turbulence) could give rise to the generation of secondary instabilities either through nonlinear interactions or transient growth. Dedicated studies of these mechanisms should be pursued.

A simplified numerical model was used to gain a preliminary handle on the expected control performance and confirm the working principle. Although the captured trends and order of magnitude for transition delay/advancement were satisfactory, ample room for improvement remains for such models, mainly in incorporating non-parallel and nonlinear theories. Notwithstanding the level of approximation, simple, fast and robust models are indispensable for the design of this type of control concept and experiment.

Finally, a key point is the future upscaling of the plasma forcing to higher Reynolds numbers. In the present study, the employed actuator was relatively weak and positioned in the simplest possible fashion (i.e. aligned to the leading edge in a straight line). Higher overall momentum coefficients can be achieved by increasing the dielectric thickness, applied voltage and number of successive actuators. Additionally, a technique enabled by the proposed automated electrode fabrication can be the use of curved electrodes, which follow the shape of the inviscid streamline, further optimising the forcing to fully counteract the CF component.

Acknowledgement

S.Y.V. is funded by the French Government programme 'Investissements d'Avenir' (LABEX INTERACTIFS, reference ANR-11-LABX-0017-01).

References

BENARD, N. & MOREAU, E. 2014 Electrical and mechanical characteristics of surface AC dielectric barrier discharge plasma actuators applied to airflow control. *Exp. Fluids* **55** (11), 1–43.

BENARD, N., NOTÉ, P. & MOREAU, E. 2017 Highly time-resolved investigation of the electric wind caused by surface DBD at various ac frequencies. *J. Electrostat.* **88**, 41–48.

CORKE, T. C., ENLOE, C. L. & WILKINSON, S. P. 2010 Dielectric barrier discharge plasma actuators for flow control. *Annu. Rev. Fluid Mech.* **42**, 505–529.

DÖRR, P. C. & KLOKER, M. J. 2015*a* Numerical investigation of plasma-actuator force-term estimations from flow experiments. *J. Phys.* D **48** (39), 395203.

DÖRR, P. C. & KLOKER, M. J. 2015*b* Stabilisation of a three-dimensional boundary layer by base-flow manipulation using plasma actuators. *J. Phys.* D*: Appl. Phys.* **48**, 285205.

DÖRR, P. C. & KLOKER, M. J. 2016 Transition control in a three-dimensional boundary layer by direct attenuation of nonlinear crossflow vortices using plasma actuators. *Intl J. Heat Fluid Flow* 449–465.

DOWNS, R. S. III & WHITE, E. B. 2013 Free-stream turbulence and the development of cross-flow disturbances. *J. Fluid Mech.* **735**, 347–380.

JOSLIN, R. D. 1998 Aircraft laminar flow control. *Annu. Rev. Fluid Mech.* **30** (1), 1–29.

KOTSONIS, M., GHAEMI, S., VELDHUIS, L. & SCARANO, F. 2011 Measurement of the body force field of plasma actuators. *J. Phys.* D*: Appl. Phys.* **44** (4), 045204.

LOVIG, E. N., DOWNS, R. S. & WHITE, E. B. 2014 Passive laminar flow control at low turbulence levels. *AIAA J.* **52** (5), 1072–1075.

MADEN, I., MADUTA, R., KRIEGSEIS, J., JAKIRLI, S., SCHWARZ, C., GRUNDMANN, S. & TROPEA, C. 2013 Experimental and computational study of the flow induced by a plasma actuator. *Intl J. Heat Fluid Flow* **41**, 80–89.

MESSING, R. & KLOKER, M. J. 2010 Investigation of suction for laminar flow control of three-dimensional boundary layers. *J. Fluid Mech.* **658**, 117–147.

SAEED, T. I., MUGHAL, M. S. & MORRISON, J. F. 2016 The interaction of a swept-wing boundary layer with surface excrescences. In *AIAA Paper* 2016-2065.

SARIC, W. S., CARPENTER, A. L. & REED, H. L. 2011 Passive control of transition in three-dimensional boundary layers, with emphasis on discrete roughness elements. *Phil. Trans. R. Soc. Lond.* A **369** (1940), 1352–1364.

SARIC, W. S., REED, H. L. & WHITE, E. B. 2003 Stability and transition of three-dimensional boundary layers. *Annu. Rev. Fluid Mech.* **35** (1), 413–440.

SARIC, W. S., WEST, D. E., TUFTS, M. W. & REED, H. L. 2015 Flight test experiments on discrete roughness element technology for laminar flow control. In *AIAA Paper* 2015-0539.

SCHUELE, C. Y., CORKE, T. C. & MATLIS, E. 2013 Control of stationary cross-flow modes in a mach 3.5 boundary layer using patterned passive and active roughness. *J. Fluid Mech.* **718**, 5–38.

SERPIERI, J. & KOTSONIS, M. 2016 Three-dimensional organisation of primary and secondary crossflow instability. *J. Fluid Mech.* **799**, 200–245.

SERPIERI, J., YADALA VENKATA, S. & KOTSONIS, M. 2017 Conditioning of cross-flow instability modes using dielectric barrier discharge plasma actuators. *J. Fluid Mech.* **833**, 164–205.

SHAHRIARI, N. 2016 On stability and receptivity of boundary-layer flows. PhD thesis, KTH Royal Institute of Technology, Stockholm, Sweden.

WANG, J. J., CHOI, K. S., FENG, L. H., JUKES, T. N. & WHALLEY, R. D. 2013 Recent developments in DBD plasma flow control. *Prog. Aerosp. Sci.* **62**, 52–78.

WANG, Z., WANG, L. & FU, S. 2017 Control of stationary crossflow modes in swept Hiemenz flows with dielectric barrier discharge plasma actuators. *Phys. Fluids* **29** (9), 094105.

WASSERMANN, P. & KLOKER, M. J. 2002 Mechanisms and passive control of crossflow-vortex-induced transition in a three-dimensional boundary layer. *J. Fluid Mech.* **456**, 49–84.